

Peak ependymal cell stretch overlaps with the onset location of periventricular white matter lesions

Valery Visser

Eindhoven University of Technology

Henry Rusinek

New York University Grossman School of Medicine

Johannes Weickenmeier (✉ jweicken@stevens.edu)

Stevens Institute of Technology <https://orcid.org/0000-0003-1889-5976>

Article

Keywords: Diffuse vascular degeneration, Primary Brain-fluid Interface, Hemodynamic Cycle, Ependymal Cell Stretch, Ventricular Walls

Posted Date: August 18th, 2021

DOI: <https://doi.org/10.21203/rs.3.rs-635671/v2>

License: © ⓘ This work is licensed under a Creative Commons Attribution 4.0 International License.

[Read Full License](#)

Peak ependymal cell stretch overlaps with the onset location of periventricular white matter lesions

Valery L. Visser^{1,2}, Henry Rusinek³, Johannes Weickenmeier^{1,*}

¹ Department of Mechanical Engineering, Stevens Institute of Technology, Hoboken, NJ 07030

² Department of Biomedical Engineering, Eindhoven University of Technology, 5600 MB Eindhoven, The Netherlands

³ Department of Radiology, New York University Grossman School of Medicine, New York, NY 10016

* Corresponding Author. Email: jweicken@stevens.edu

Abstract

Deep and periventricular white matter hyperintensities (dWMH/pvWMH) are bright appearing white matter tissue lesions in T2-weighted fluid attenuated inversion recovery magnetic resonance images and are frequent observations in the aging human brain. While early stages of these white matter lesions are only weakly associated with cognitive impairment, their progressive growth is a strong indicator for long-term functional decline. DWMHs are typically associated with vascular degeneration in diffuse white matter locations; for pvWMHs, however, no unifying theory exists to explain their consistent onset around the horns of the lateral ventricles. We use patient imaging data to create anatomically accurate finite element models of the lateral ventricles, white and gray matter, and cerebrospinal fluid, as well as to reconstruct their WMH volumes. We simulated the mechanical loading of the ependymal cells forming the primary brain-fluid interface, the ventricular wall, and its surrounding tissues at peak ventricular pressure during the hemodynamic cycle. We observe that both the maximum principal tissue strain and the largest ependymal cell stretch consistently localize in the anterior and posterior horns. Our simulations show that ependymal cells experience a loading state that causes the ventricular wall to be *stretched thin*. Moreover, we show that maximum wall loading coincides with the pvWMH locations observed in our patient scans. These results warrant further analysis of white matter pathology in the periventricular zone that includes a mechanics-driven deterioration model for the ventricular wall.

1 Introduction

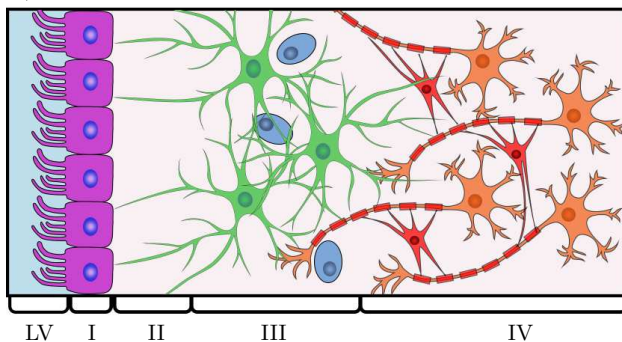
White matter hyperintensities (WMH) are bright appearing white matter tissue lesions in T2-weighted fluid attenuated inversion recovery (FLAIR) magnetic resonance imaging (MRI) [1, 2, 3] and are a frequent observation in the aging human brain [4, 5]. WMHs have been linked to vascular degeneration during aging [3, 6] and multiple sclerosis [7, 8]. It is typically described that hypertension [9, 10], smoking [11, 12], diabetes [13, 14], and heart disease [15, 10] are common risk factors that exacerbate the vascular involvement leading to white matter changes. WMHs are classified as deep white matter hyperintensities (dWMH) and periventricular white matter hyperintensities (pvWMH) on the basis of anatomical localization [16]. While cerebral ischemia and small vessel disease are the primary pathophysiological observations in WMHs [3, 6, 17, 18], we pose here, that the onset of pvWMHs is subject to additional mechanical damage mechanisms. We expect that a lifetime of cyclic mechanical of the ependymal cells lining the ventricular wall due to a combination of hemodynamic forces and CSF flow leads to cell damage, structural degeneration of the lateral ventricular wall, and its progressive functional failure. Here, as a first step, we use a finite element modeling approach to show that ependymal cells experience peak mechanical loading in the ventricular horns that co-localizes with WMH masks based on clinical patient data. The finite element modeling approach is particularly useful because it allows us to create anatomically accurate brain models of various ventricle shapes to demonstrate that ependymal cell stretch patterns are consistent across subjects.

Clinically, WMHs are a common observation in medical images of the elderly and their severity typically increases with age [19, 20, 21]. By the age of 44, there is a 50.9% likelihood of incidental WMH findings in healthy, cognitively normal subjects [22] and by age 60, nearly every brain exhibits signs of white matter lesions [23, 24]. While early stages of these white matter lesions are only weakly associated with cognitive impairment [25], the accumulation and expansion of white matter lesions is considered a reliable indicator for long-term functional decline [26, 27]. In particular, the volume of pvWMHs is associated with accelerated functional decline [28].

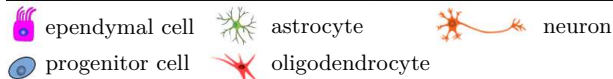
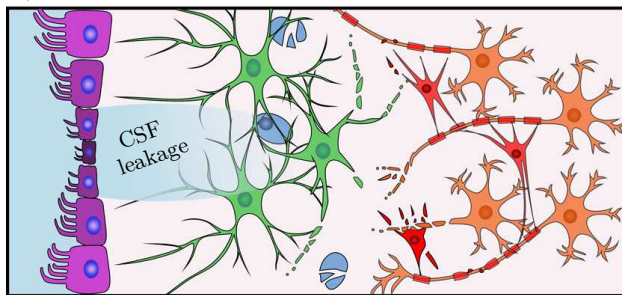
The pathophysiology of white matter lesions is poorly understood, but is strongly linked to location. PVWMHs are much more likely to be observed in the aging brain than dWMHs. DWMHs are linked to ischaemic damage, hypoxia, and hypoperfusion [29, 30]. Although pvWMHs are associated with ischaemia of perforating arterioles as well, they are further characterized by ependymal cell thinning, leakage of cerebrospinal fluid (CSF) into the tissue behind the ventricular wall, and, as inflammatory processes expand, manifests as demyelination, axonal loss, reduced glial density, tissue atrophy [31, 32, 33, 34], and the formation of astroglial scarring [35, 36, 37]. Fazekas et al. reported that pvWMHs consistently first appear in the ventricular horns and expand towards deep white matter tissue over time [1]. This observation is reflected in the evaluation criteria proposed by Fazekas et al. yielding a score from 1 to 3. The Fazekas score (FS) differentiates between *caps* or *pencil-thin linings* in the horns associated with the earliest manifestation of pvWMHs (FS=1), *smooth halos* linked to progressively growing pvWMH volumes (FS=2), and ultimately *irregular periventricular signal* that extends into deep white matter (FS=3) [1]. Incidental white matter findings in young healthy adults further support the notion that pvWMHs first emerge in ventricular horns [22]. To date, however, no theory has been proposed to explain the underlying mechanism. Moreover, temporal changes of white matter lesions are poorly understood [38]. White matter lesion volume has been shown to grow on average by 14.6% per year in dWMH and by 9.9% per year in pvWMH [39]. There remain critical knowledge gaps, however, in explaining WMH volume growth over time and the progressive expansion of WMHs along the ventricular wall, on the one hand, and the diffusion of CSF and white matter inflammation radiating out from the ventricular horns into deep white matter on the other.

Anatomically, the ventricular epithelium is lined by the ependymal wall that is composed of distinct layers, see Figure 1, with varying thicknesses and densities as shown in Figure 1. Going from ventricle towards brain parenchyma, one observes a monolayer of cuboidal multiciliated ependymal cells (Layer I), a prominent hypocellular gap very rich in processes from ependymal cells and astrocytes (Layer II), a ribbon of cells composed of astrocytes (Layer III), and a transitional zone into the brain parenchyma (Layer IV) [40]. A) In a healthy state, the ependymal wall regulates the exchange of fluid and nutrients between the lateral ventricle and brain tissue. B) With age, the thin layer of ependymal cells degrades leading to the unregulated influx of CSF into the hypocellular layer first and deeper white matter tissue next. Once breached, white matter lesions emerge and propagate. C) Given the morphology of the ventricular wall, ependymal cells are *stretched thin* due to pulsatile fluid flow in the lateral ventricles [32].

a) schematic anatomy of the *healthy* ependymal wall



b) schematic anatomy of the *degenerating* ependymal wall



c) ependymal cell tension λ_t and cell compression λ_c

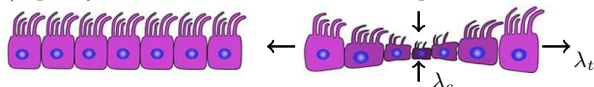


Figure 1: The ventricular epithelium is a functional barrier between the brain and CSF. It consists of four distinct layers: a monolayer of cuboidal multiciliated ependymal cells (Layer I), a prominent hypocellular gap very rich in processes from ependymal cells and astrocytes (Layer II), a ribbon of cells composed of astrocytes (Layer III), and a transitional zone into the brain parenchyma (Layer IV) [40]. A) In a healthy state, the ependymal wall regulates the exchange of fluid and nutrients between the lateral ventricle and brain tissue. B) With age, the thin layer of ependymal cells degrades leading to the unregulated influx of CSF into the hypocellular layer first and deeper white matter tissue next. Once breached, white matter lesions emerge and propagate. C) Given the morphology of the ventricular wall, ependymal cells are *stretched thin* due to pulsatile fluid flow in the lateral ventricles [32].

cells composed of astrocytes (Layer III), and a transitional zone into the brain parenchyma (Layer IV) [40]. The multiciliated ependymal cells in Layer I are tightly joined by connexins and cadherins, or gap junction proteins, which form tight inter-cellular connections [33]. Layer II is present in the entire ependymal wall in the lateral ventricles, but varies in thickness from region to region. The presence of aquaporin 4 in the basolateral plasma membranes of ependymal cells results in a directed water flow [41]. Aquaporin 4 junctions facilitate the reabsorption of interstitial fluid into the parenchymal vasculature [42] and drive the unidirectional fluid drainage into ventricular spaces [41]. If the ependyma is disrupted (Figure 1B), reactive astrocytes will line the ventricular wall in an attempt to reestablish homeostasis [33, 35]. The reactive replacement of ependymal wall with gliotic tissue is associated with the lack of polarized aquaporin 4 junctions. This leads to an undirected transport of CSF through the ependyma [35, 34]. Over time, the dysregulated CSF-brain parenchyma barriers leads to excessive influx of CSF into the hypocoelular layer and the accumulation of fluid and dysregulated homeostasis [43].

Computational modeling of the mechanical loading state of the ventricular wall is a suitable approach to demonstrate the consistent localization of maximum wall loading in the ventricular horns irrespective of ventricle size. Here, we combine subject-specific finite element model generation via medical image segmentation with FLAIR image-derived WMH masks to test our proposed damage mechanisms. Previous computational models of the (peri)ventricular space primarily focused on assessing hydrocephalus [44, 45, 46, 47, 48] or white matter damage during traumatic brain injury [49]. While these models provide valuable insight into organ-level tissue response, they are unsuitable to determine the cellular loading state along the ventricular wall and in the ventricular horns. Our present contribution consists of the generation of eight subject-specific, anatomically accurate finite element models of a representative axial brain section in order to identify the locations of maximum loading along the ventricular wall. We subsequently compare wall loading at peak hemodynamic pressure with the locations of pvWMHs observed in the subject’s accompanying medical scans. We show that peak ependymal cell loading nearly always coincides with pvWMH locations in our cohort. Thus, we suggest that the mechanical loading of ependymal cells is one of the most important risk factors for the emergence of pvWMHs and is a physics-based mechanism to explain the gradual growth of pvWMH into deep white matter tissue.

2 Methods

2.1 Image selection and WMH segmentation

We obtained magnetic resonance images (MRI) from cognitively normal subjects in the imaging database of the New York University Alzheimer’s Disease Research Center (NYU ADRC). The standardized MRI protocol included FLAIR and high-resolution structural MPRAGE volumetric sequences. We separated the 464 active subjects by gender and sorted them based on their total intracranial CSF volume [50]. To capture a broad range of ventricular geometries, we selected male and female subjects from the 20th, 40th, 60th, and 80th percentile of CSF volume, as shown in Figure 3, which are labeled as F20/F40/F60/F80 (females) and M20/M40/M60/M80 (males), respectively. Our subjects are on average 73.4 ± 5.9 years of age. From a mechanics perspective, 8 subjects is a reasonable sample size to demonstrate the repeatable ependymal cell loading state along the ventricular wall across a wide range of ventricular shapes. For all eight subjects, a white matter hyperintensity (WMH) mask was obtained based on their FLAIR images using the freely available software package FireVoxel [www.firevoxel.org] following the procedure described by Chen et al. [51]. Briefly, the algorithm estimates the mean signal intensity μ and the standard deviation σ of FLAIR signal s within the brain region Ω . White matter hyperintensity masks are computed as $\{v \mid v \in \Omega \wedge s(v) > \mu + k\sigma\}$, where k was set at 2.5. WMH masks were provided in the form of binarized images registered to the subjects’ MRI.

2.2 Finite Element Model Generation

We generated personalized finite element models of each subject based on a semi-automatic segmentation approach. We segmented each structural MR image using Freesurfer and imported both, the structural scan and the Freesurfer segmentation, into the 3D image processing and model generation software SimplewareTM

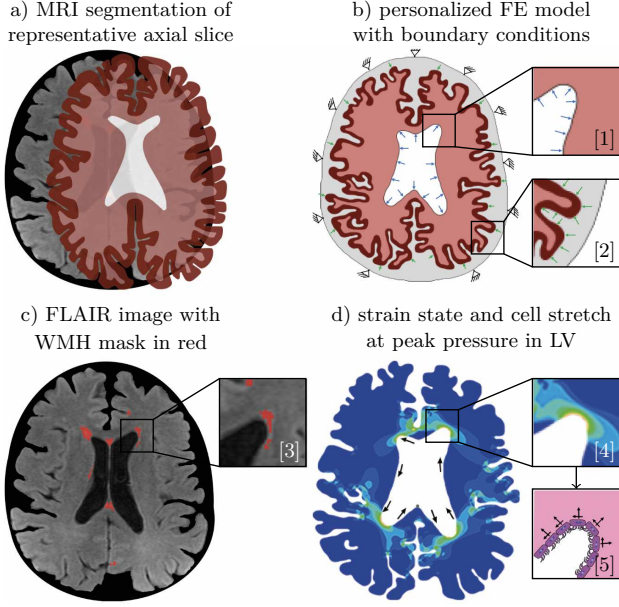


Figure 2: We generated finite element models for each subject individually by segmenting axial MRI through the lateral ventricle. A) We identified the boundaries of gray matter, white matter, lateral ventricles, and cerebral spinal fluid surrounding the cortex. B) The model was kinematically constrained along the outer boundary, and we applied a pressure normal to the ventricular wall (B1) and normal to the outer gray matter surface (B2). C) Accompanying FLAIR images superposed with a mask of white matter hyperintensities show the localization of early leukoaraiosis in the ventricular horns (C3). We simulated peak loading during the hemodynamic pressure cycle in order to obtain the strain field (D4) and ependymal cell stretch along the ventricular wall (D5).

(Synopsys, Inc., Mountain View, CA) [52, 53, 54]. We identified the axial slice with the largest ventricular area showing the anterior and posterior horns and manually corrected the imported Freesurfer segmentation of the lateral ventricle, white and gray matter, and surrounding CSF based on the co-registered structural scan. Figure 2 shows the model generation process. Using the FE Module of Simpleware, we converted our segmentations into finite element meshes and imported our models into Abaqus (Dassault Systèmes, Providence, RI). We constrained our model against out-of-plane deformations (plane strain simulation) and applied pressure boundary conditions to two surfaces: a normal pressure to the ventricular wall (green arrows in Figure 2B1) and a normal pressure to the gray matter-CSF interface (blue arrows in Figure 2B2). These loading conditions represent the cyclic brain deformations caused by a combination of hemodynamic forces and CSF flow [55]. The lateral ventricles, in particular, undergo a piston-like motion causing cyclic volumetric expansion during systole [56]. To that end, we prescribed an LV pressure of 20 Pa, or 0.15 mmHg, and an SAS pressure of 1 Pa, or 0.0075 mmHg, in line with observations that SAS pressure is only 10-20% of the ventricular pressure [57, 58, 59, 60]. We mimic the skull, which is orders of magnitudes stiffer than cerebral tissues, by prescribing zero-displacement boundary conditions, shown in gray in Figure 2, on the outer periphery of our model. We do not model fluid flow around the brain as well as fluid flow and CSF production in the ventricles, but assume fluid cavities to expand and contract with each heartbeat. Therefore, we approximate CSF as an ultrasoft, compressible material with a Young's modulus of 0.1 kPa and a Poisson's ratio of 0.3. Brain tissues were modeled as an Ogden-type hyperelastic material model [61, 62]. Following basic continuum theory of finite deformations, we introduce the deformation gradient \mathbf{F} as the gradient of the nonlinear deformation field ϕ with respect to the material coordinates \mathbf{X} in the reference configuration. Assuming nearly incompressible behavior of brain tissue, we decompose the deformation gradient \mathbf{F} into a volumetric contribution characterized through the Jacobian J and an isochoric contribution $\bar{\mathbf{F}}$,

$$\mathbf{F} = \nabla_{\mathbf{X}}\phi = J^{1/3}\bar{\mathbf{F}}, \quad \text{with } J = \det(\mathbf{F}) \quad \text{and} \quad \bar{\mathbf{F}} = J^{-1/3}\mathbf{F}. \quad (1)$$

As a characteristic deformation measure, we introduce the right Cauchy-Green deformation tensor \mathbf{C} which obeys a similar decomposition into a volumetric contribution in terms of the Jacobian J and an isochoric contribution $\bar{\mathbf{C}}$,

$$\mathbf{C} = \mathbf{F}^T \cdot \mathbf{F} = J^{2/3}\bar{\mathbf{C}}, \quad \text{with } J^{2/3} = \det^{2/3}(\mathbf{F}) \quad \text{and} \quad \bar{\mathbf{C}} = \bar{\mathbf{F}}^T\bar{\mathbf{F}}. \quad (2)$$

We can then introduce the isochoric first and second invariants, \bar{I}_1 and \bar{I}_2 , either in terms of the isochoric right Cauchy-Green deformation tensor $\bar{\mathbf{C}}$, or in terms of the isochoric principal stretches $\bar{\lambda}_1$, $\bar{\lambda}_2$, and $\bar{\lambda}_3$,

recalling that $\bar{I}_3 = J^2 = 1$,

$$\begin{aligned}\bar{I}_1 &= \text{tr}(\bar{\mathbf{C}}) = \bar{\lambda}_1^2 + \bar{\lambda}_2^2 + \bar{\lambda}_3^2, \\ \bar{I}_2 &= \frac{1}{2}[\text{tr}^2(\bar{\mathbf{C}}) - \text{tr}(\bar{\mathbf{C}}^2)] = \bar{\lambda}_1^2\bar{\lambda}_1^2 + \bar{\lambda}_2^2\bar{\lambda}_1^3 + \bar{\lambda}_3^1\bar{\lambda}_1^2.\end{aligned}\tag{3}$$

It has been shown that the mechanical response of brain tissue is best captured by a one-term Ogden model given by the strain energy density function, Ψ , [61]

$$\Psi = \frac{\mu}{2}[\bar{\lambda}_1^2 + \bar{\lambda}_2^2 + \bar{\lambda}_3^2 - 3] + \frac{\kappa}{4}[J^2 - 1 - 2 \log(J)],\tag{4}$$

with shear modulus μ governing isochoric, distortional deformations and bulk modulus κ governing dilatational deformation. We assume our material to be nearly incompressible with a Poisson's ratio of 0.45 and a white-gray matter stiffness ratio of 2 [61]. Specifically, we chose experimentally-informed constants $\mu = 0.34$ kPa and $\kappa = 0.0033$ kPa for gray matter and $\mu = 0.68$ kPa and $\kappa = 0.0067$ kPa for white matter [57, 61, 63, 64, 65]. We implemented the Ogden model in a user material subroutine (UMAT) following the example of [62] and compute ventricular wall stretches as outlined further below.

2.3 Ventricular geometry as a measure for WMH severity

We propose two measures for the analysis of horn geometry and its impact on WMH severity. For each horn, we fit a circle through three points: the location of maximum cell tension, and the two locations left and right of this point where cell tension has dropped to 10% of the maximum value. We measure the radius r of the sphere as a critical measure for horn geometry. Mechanically, curvature κ , which is inversely proportional to horn radius r with $\kappa = 1/r$, directly correlates with cell tension and cell compression. Ventricles with small horn radius, that is with smaller volumes, are characterized by increased ependymal cell stretches; therefore, horn radius provides a predictive measure for the severity of cellular loading. Biologically, horn radius increases with age due to ventricular enlargement caused by tissue degeneration. We also determine the sections of the ventricular wall that are exposed to cell stretches above 10% of the maximum value. Specifically, we measure the length of the ventricular wall exposed to this critical cell stretch for each horn and divide this measure by the total wall length. The resulting measure provides the wall fraction with stretch exceeding a damaging ependymal cell stretch level.

2.4 Mechanomarkers for WMH formation

The ventricular wall is lined with cuboidal multiciliated cells that are tightly connected by cadherin junctions [32, 33]. Our proposed damage mechanism rests on the hypothesis that ependymal cells experience a mechanical loading state that compromises their integrity. Specifically, we submit that the intercellular connections are particularly vulnerable to mechanical deformations and that their increased loading ultimately leads to failure and the leakage of CSF into the surrounding white matter, which appears as hyperintensities in FLAIR images. To that end, we determine cellular deformations and differentiate between ependymal cell tension in the direction tangential to the ventricular wall and ependymal cell compression in the direction normal to the ventricular wall, see Figure 2d5. We determine the normal and tangential wall directions from a Laplacian diffusion simulation for each of our eight FE models. We prescribe a temperature boundary condition of 1.0°C on the nodes outlining the ventricular wall, 0.2°C on the interface between gray and white matter, and of 0.0°C for all nodes on the interface between gray matter and CSF. The resulting flux field allows us to identify the directions of the steepest temperature gradient \mathbf{n}_0 , normal to the undeformed ventricular wall, and isothermes \mathbf{t}_0 , tangential to the undeformed ventricular wall. We import the two vector fields into our simulations and project the right Cauchy-Green deformation tensor \mathbf{C} onto these directions to obtain cell tension and cell compression. Specifically, we calculate the right Cauchy-Green strain tensor and project strains onto the normal and tangential directions, respectively,

$$\lambda_t = \sqrt{\mathbf{t}_0 \cdot \mathbf{C} \mathbf{t}_0} \quad \text{and} \quad \lambda_c = \sqrt{\mathbf{n}_0 \cdot \mathbf{C} \mathbf{n}_0}.\tag{5}$$

During post-processing of each simulation, we identify the nodes lining the ventricular wall, starting at the midpoint between the two posterior horns of the lateral ventricle and move counter-clockwise along the ventricular wall, see Figure 2d5. We then determine ependymal cell tension and ependymal cell compression in

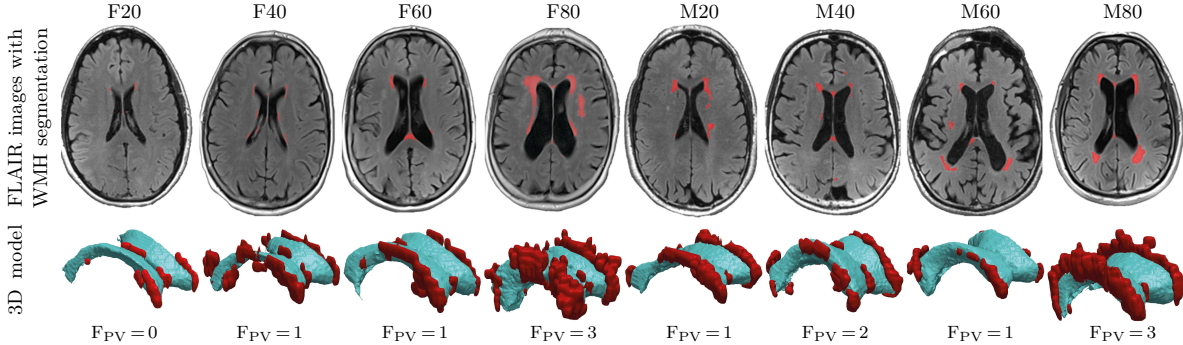


Figure 3: Representative axial slices and volumetric reconstructions of lateral ventricles and white matter hyperintensities from eight subjects. We sorted 464 subjects from the NYU ADRC’s imaging database based on their total intracranial CSF volume and picked a male and female subject from the 20th, 40th, 60th, and 80th percentile. The top row shows the FLAIR MRI sequence of all eight patients with a white matter hyperintensity mask (red); the bottom row shows volumetric reconstructions of their ventricles (blue) and white matter hyperintensities (red). We also provide the Fazekas score of the periventricular WMHs.

subject	age [y]	vCSF [cm ³]	vLV [cm ³]	vWMH [cm ³]	FS
F20	65.1	421.0	30.2	1.1	0
F40	68.5	473.0	34.2	5.2	1
F60	75.3	519.0	40.1	4.0	1
F80	77.6	579.0	74.1	20.7	3
M20	68.5	451.0	33.4	6.2	1
M40	81.1	493.0	35.3	7.8	2
M60	79.9	519.0	56.9	7.0	1
M80	71.4	581.0	61.4	16.4	3

Table 1: Summary of subject data including age, CSF volume (vCSF), lateral ventricle volume (vLV), WMH volume (vWMH), and Fazekas score (FS). We selected eight representative cognitively normal subjects from the 20th, 40th, 60th, and 80th percentile of CSF volume.

each node to arrive at the representations shown in Figures 5 and 6. Furthermore, we compute the maximum principal strains (MPS) from the Green-Lagrange strain field given by $\mathbf{E} = 1/2(\mathbf{C} - \mathbf{I})$, with identity tensor \mathbf{I} . As shown in Figure 5, MPS is a representative measure for tissue loading in the vicinity of the ventricular wall and takes on a similar outline as the WMH mask.

3 Results

3.1 Morphological changes of the lateral ventricles

Table 1 lists age, CSF, LV, WMH volumes, and Fazekas score for each subject. CSF, LV, and WMH volumes were determined via FireVoxel [51]. CSF volumes range from 421 cm³ (20th percentile) to 581 cm³ (80th percentile). Lateral ventricle volumes (vLV) range from 14 cm³ (20th percentile) to 74 cm³ (80th percentile) with an average vLV of 45.7±16.2 cm³. WMH volumes range from 1.1 cm³ to 20.7 cm³ with an average volume of 8.55±6.6 cm³. In spite of a small sample size we observe significant correlations between lateral ventricle volume and Fazekas score (Pearson’s correlation coefficient $r(8) = 0.77$, $p = 0.026$) as well as WMH volume and Fazekas score ($r(8) = 0.95$, $p < 0.001$). In males, WMH volume is 1.2 times larger than in females with a mean WMH volume of 9.4 cm³ for male subjects and 7.8 cm³ for female subjects. Figure 3 shows WMH caps around the anterior horns for F/M20, smooth WMH halos for F/M40-60, and increasingly diffuse and deep-reaching WMHs for F/M80.

When we fitted a circle into each of the horns in our eight models, we observe that horn radius consistently

increases with vCSF and vWMH. Figure 4 shows the relationships between averaged horn radius per subject (markers shows mean horn radius with horizontal lines indicating the standard deviation) and CSF (blue data) and WMH volumes (red data). Based on a linear fit through both data sets, we observe an R^2 values of 0.822 with $p = 0.00189$ for vCSF and an R^2 value of 0.443 with $p = 0.0718$ for vWMH. An increasing horn radius is a characteristic morphological manifestation of aging brains which undergo significant cerebral atrophy and ventricular enlargement. [10, 31, 66].

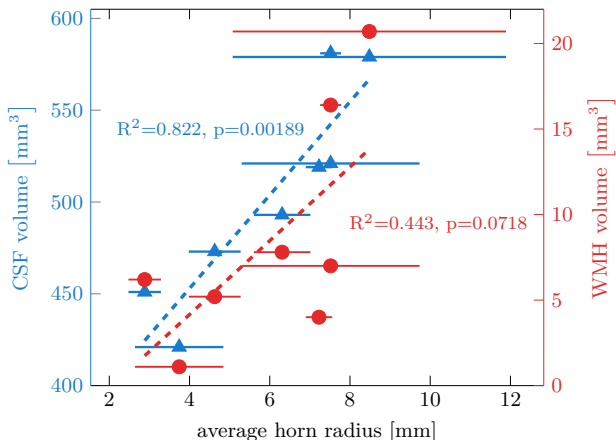


Figure 4: Horn radius versus CSF volume and WMH volume. We show the average of all four horn radii for each subject (marker with standard deviation as a horizontal line). We observe an overall increase of horn radius with increasing CSF and WMH volumes.

3.2 Ependymal cell stretch along the ventricular wall

Figure 5 shows the WMH mask in FLAIR images of our eight subjects, the maximum principal strain, and the computed ependymal cell stretches (EC stretch), associated with cell tension (elongation) and cell compression (thinning), see Figure 1c. The maximum principal strain field is highest at the edge of the ventricles and diffuses towards deeper white matter. We observe a significant increase in maximum EC stretch in ventricular horns, with maximum cell tension of up to 1.07 in female and 1.08 in male subjects; maximum thinning occurs in the same locations where we observe cell compression of up to 6% in female and 7% in male subjects. All eight subjects show a similar pattern of four sharp focal points with significantly increased cell stretches in both tension and compression. The locations of the four focal points coincide with the anterior and posterior horns of the lateral ventricles.

We use a two-sample T-test to demonstrate different (elevated) EC stretch in the presence of pvWMHs. To obtain an independent data set, we sample tangential EC stretch at 30 equidistant points along the ventricular wall. We differentiate between cell stretch at points where pvWMHs are present ($n=41$) and compare them to the cell stretch where there are no pvWMHs ($n=199$). The T-test reveals a significantly higher EC stretch where there are pvWMHs with $t(49) = 3.58$ and $p = 0.00039$.

4 Discussion

4.1 Patient-specific simulation of ventricular wall loading

We determine ependymal cell tension (tangential to wall) and ependymal cell compression (normal to the wall) by projecting the right Cauchy-Green deformation tensor onto the principal directions of the ependymal cells lining the ventricular wall. Despite pronounced variations in lateral ventricle geometry across our subjects, as Figure 6 shows, peak cell tension and cell compression consistently localize in the anterior (B, C) and posterior (A, D) horns. Comparison with the location of pvWMHs along the ventricular wall, as shown in Figure 5 (bottom row), reveals that tissue damage co-localizes in regions of peak cell stretches. The loading condition in these regions leads to ependymal cells being *stretched thin* and imposes a particularly high load on intercellular cadherin junctions [33]. The exterior sides of the ventricular wall (between points A and B, and between points C and D) experience negligible cell stretches. The anterior and posterior attachment points of the septum pellucidum (the wall section between points D and A, and between points

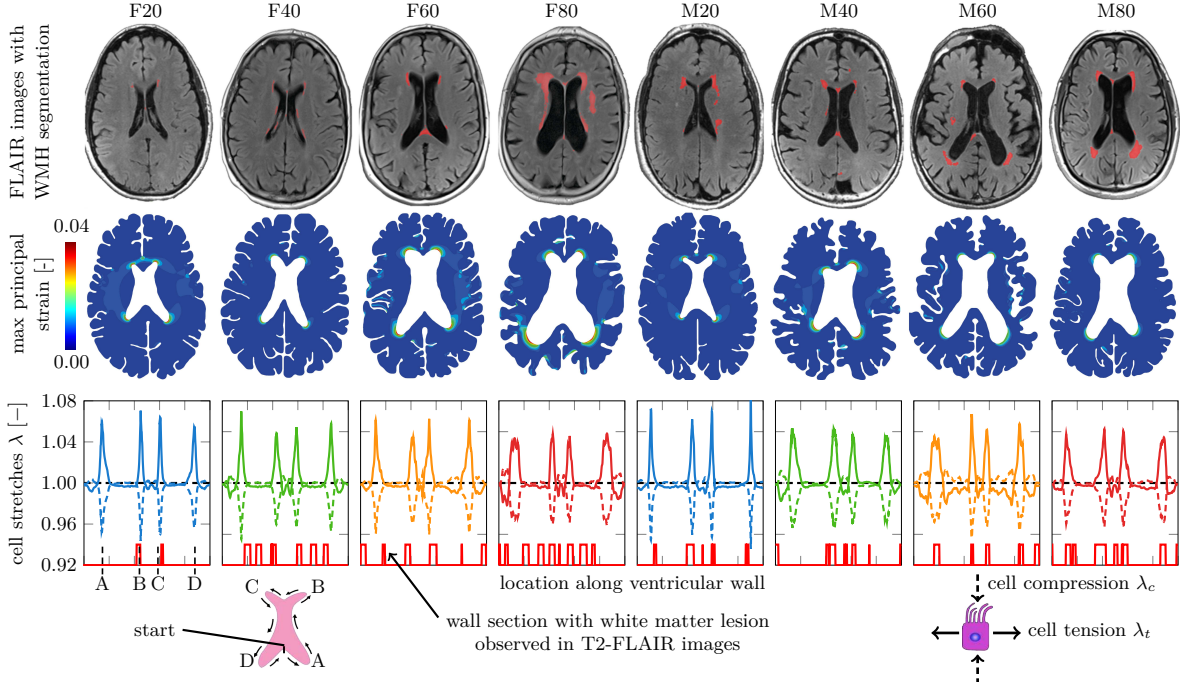


Figure 5: Eight finite element models were created from FLAIR MRI with WMHs shown in red (top row). We simulated quasistatic ventricular expansion during peak loading to determine ventricular wall strain and ependymal cell stretch. The distribution of maximum principal strain (middle row) is consistent across all individuals, with peak strain localizing around the anterior and posterior horns of the lateral ventricles. Based on the deformation fields, we determine ependymal cell stretch along the ventricular wall. We calculate ependymal cell tension, which is tangential to the ependymal wall, and ependymal cell compression, which is perpendicular to the ependymal wall. We observe four distinct locations with maximum stretches along the wall. These coincide with the horns, as indicated by points A, B, C, and D. We report both stretch components for every point along the ependymal wall as shown in the ventricular representation in the legend.

B and C) exhibit slightly elevated stretches and cause cell compaction, i.e. the opposite loading state than in the horns. Therefore, we pose that the clinical observation of pvWMHs first appearing as localized caps in the anterior and posterior horn is in part driven by the particular mechanical loading state of ependymal cells [35]. Once initiated, pvWMHs deteriorate into bright-appearing linings and ultimately deeper reaching WMHs as LV wall failure worsens and CSF diffuses into deeper white matter regions [32, 33, 43]. Based on our initial analysis, it would be possible to model the progressive deterioration of periventricular tissue and the spreading of astrogliosis after wall failure.

4.2 Ventricular deterioration changes ependymal cell loading

Despite the significant reproducibility of the cellular loading pattern shown in Figure 6, we observe distinct differences between our subjects with larger LV volume and a clear trend towards an expanding ventricular geometry. As LV volume increases and ventricular horns enlarge, cellular stretch magnitude decreases, but the region of elevated cell stretch increases in comparison to sharp peaks in younger brains. Figure 7 shows how peak cell stretch and wall fraction with elevated cell tension relate to horn radius. As ventricular volume increases, horn radii increase as well. More strikingly, in spite of the small sample size, a Spearman's rank correlation test revealed a statistically significant negative correlation between peak stretch and horn radius ($p < 0.0001$, $\rho = -0.65$). While peak ependymal cell tension magnitude decreases for increasing horn radius, we observe that the ventricular wall fraction affected by elevated stretch increases with horn radius by up to a factor 3. These observations are critical in understanding the impact of mechanical loading on the progressive deterioration of the ependymal wall [10, 31]. The ventricular geometry in young, healthy subjects is characterized by higher cell stretches. In older subjects, ependymal cells appear to experience

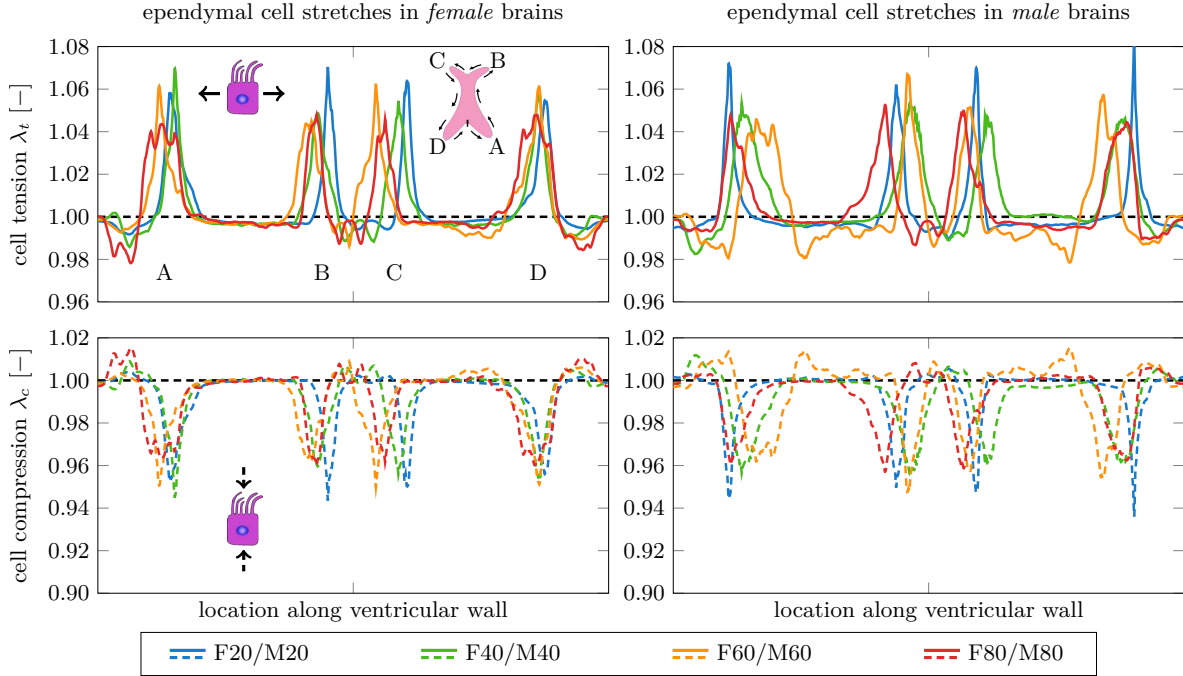


Figure 6: Subject-specific endymal cell stretches along the ventricular wall at peak hemodynamic loading. We project the local tissue strain onto the direction causing endymal cell tension tangential to the wall (top row) and endymal cell compression normal to the wall (bottom row). The combined loading state causes pronounced cell thinning and imposes significant strain on cell-cell connections. We observed a significant concentration of maximum cell loading in the anterior and posterior horns of the lateral ventricles. This observation is consistent across our cohort and gender-nonspecific.

mechanical fatigue due to their repeated mechanical loading. Accompanying cellular deterioration leads to CSF leakage into periventricular white matter and facilitates secondary tissue damage mechanisms in layers II-IV, see Figure 1. We pose that horn radius may be a reliable biomarker for the clinical assessment of a subject's risk of developing pvWMHs or leukoaraiosis [66].

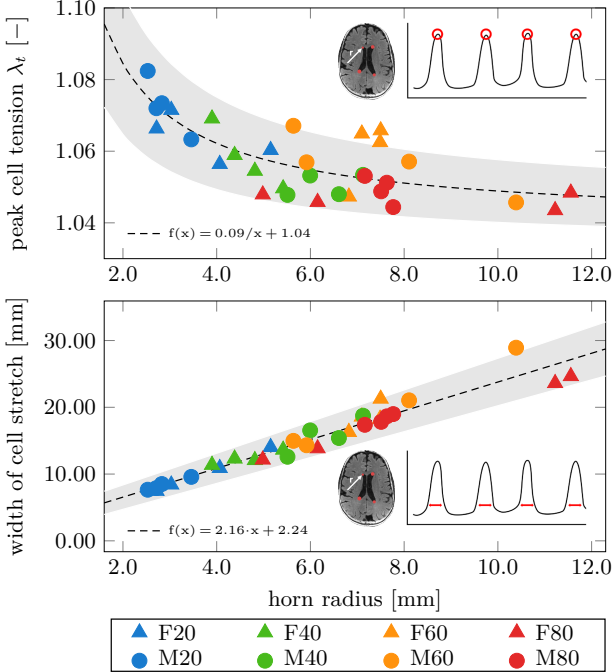


Figure 7: Ventricular geometry is an indicator for peak cell stretch (top row) and the wall fraction exposed to elevated cell stretch (bottom row). We measure the radius of a sphere fitted to the anterior and posterior horns as a representative marker for ventricular geometry. We observe that peak cell stretch decreases for increasing horn radii and that an increasing wall section experiences elevated cell stretch as horn radius increases. Our observations suggest that younger brains with sharper ventricular horns, i.e., smaller horn radii, experience higher ependymal cell loading while aged brains (with larger horn radii) experience lower cell loads but elevated stretches on larger wall sections, i.e., increased width of cell stretch.

4.3 Sensitivity analysis of model parameters

We analyzed our model’s sensitivity to ventricular wall pressure and white matter tissue stiffness, and show the results for subject F40 in Figure 8. We applied intracranial pressures of 0.5, 5, and 10 times the referential pressure of 20 Pa and observe a significant increase in the average peak cell stretch value of up to 1.56. Specifically, when applying 5-times the referential pressure, maximum cell tension increases by a factor of 1.21 and maximum cell compression increases by a factor of 1.18; when applying 10-times the referential pressure, maximum cell tension increases by a factor of 1.48 and maximum cell compression increases by a factor of 1.41. Strikingly, we observe a minimal effect on the lateral sides of the ventricular cavity and no shift in the location of peak stretches. The wall fraction exposed to increased cell tension increases with increasing pressure while the location of peak load remains unchanged. The range of ventricular pressures was based on literature reporting significant pressure variations for healthy subjects and subjects with hypertension and hydrocephalus [67, 68, 69]. This implies that subjects with increased intracranial or hemodynamic pressure are at an elevated risk to damage their ventricular wall and are more likely to develop leukoaraiosis [19].

We simulated variable tissue stiffness and compared cell stretches for white matter stiffness ranging from 25% to 400% of the original, experimentally observed stiffness to represent the range of values reported in literature [61, 64, 70]. In comparison to the variation in pressure, we observe a significantly lower effect, with a maximum 1.07-fold increase in peak cell loading, see Figure 8b. It is important to note, however, that tissue softening leads to increased cell loads. This provides further evidence that tissue degeneration is a mechanically driven mechanism that leads to accelerated tissue aging and pvWMH volume growth.

4.4 Risk factors for the onset of periventricular white matter lesions

Hydrocephalus and other neurological diseases that lead to increased intracranial and blood pressure pose a significant risk to the mechanical integrity of the ventricular wall [71, 72, 73]. It has been shown experimentally that a rapid increase in ventricular pressure leads to ependymal wall failure and the diffusion of CSF into white matter tissue [43]. Strikingly, this was observed to occur first in the ventricular horns, which agrees with our hypothesis that ependymal cells experience peak mechanical load in these locations which leads to functional failure. Therefore, our unifying physics-driven damage model explains the onset location of pvWMHs and is supported by histopathological studies on ventricle surface gliosis [74] and the observation of decreased white matter integrity [75]. Moreover, our model provides a rationale for the different stages of

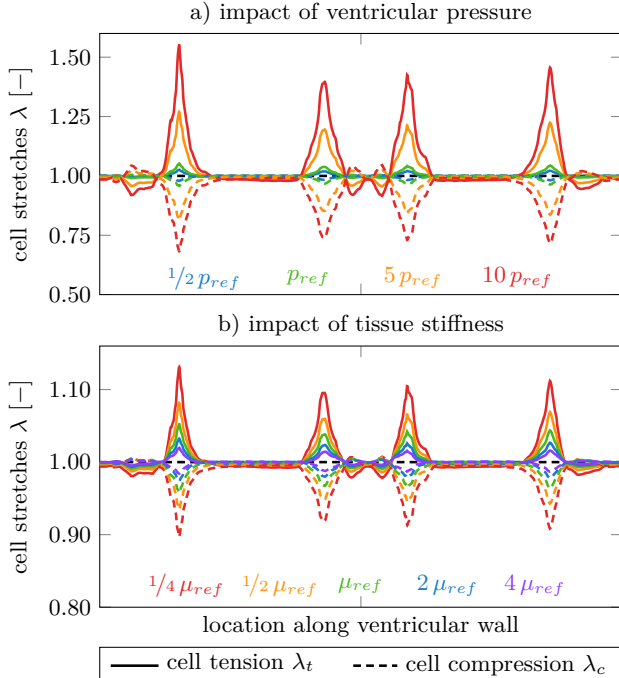


Figure 8: Sensitivity analysis of ventricular pressure level (top row) and mechanical brain tissue stiffness (bottom row) uncovers the impact on ependymal wall stretches. A ten-fold increase in referential ventricular pressure leads to cell stretch of up to 1.56 and cell compression as low as 0.71. In comparison, a four-fold increase in tissue stiffness reduces peak cell stretches by a factor 0.97 and a four-times lower shear modulus leads to a 1.07-fold increase in peak cell stretch. (All values are relative to tissue stiffness reported in the Methods section). Ventricular pressure is highly heterogeneous across subjects [69]. As discussed in the next section, ventricular pressure appears to be the critical parameter in the etiology of ependymal cell fatigue.

pvWMHs as they evolve in parallel with the extended strain field observed in our simulations. Clearly, aging and small vessel disease are important risk factor as well. Peak wall loading in the form of ependymal cell thinning occurs in the horns and extends radially into deeper white matter. Lateral sides of the ventricles are exposed to negligible loads and are subsequently more protected [74]. Once the ventricular wall is disrupted, ependymal wall layers II-IV experience CSF influx and tissue damage due to inflammation and astrogliosis [32, 34]. It was shown that astrocytes cover the denuded ventricular walls of hydrocephalic hyh mutant mice to form a new cell layer with a cell organization that resembles the ependyma [38]. The fluid accumulation in the hypocellular layer triggers subsequent damage mechanisms such as astroglial scarring and the depletion of progenitor cells, which are required for tissue regeneration [37, 38]. PVWMHs first appear as caps in the ventricular horns and are independent of a subject’s ventricular shape at the time of onset. Although vascular damage is a driving force in WMHs, the consistent localization in horns suggests the involvement of additional factors. Based on our mechanics-driven hypothesis, sharp horns, i.e., small horn radii, cause high ependymal cell loads and therefore represent a critical additional risk factor for wall failure.

4.5 Mechanomarker for periventricular white matter hyperintensities

Our numerical modeling approach shows best agreement between EC stretch and pvWMH location for early stages of pvWMH formation, i.e., models M/F20 and M/F40. As pvWMHs increase and penetrate into deeper white matter regions, our current model requires additional mechanisms to propagate tissue deterioration from the ventricular wall into deeper layers of the periventricular zone. Specifically, our model requires a constitutive damage mechanism to quantify the degree of ependymal cell fatigue in order to trigger local tissue softening and the subsequent expansion of the critically loaded wall segments [76]. Distinct structural brain changes, such as cerebral atrophy [77, 78] or white matter pathology [79], are useful biomarkers for diagnosis of abnormal aging. Our model establishes ependymal cell loading as a mechanomarker for periventricular white matter lesion location. Cell loading magnitude is directly affected by ventricular pressure and LV shape. Therefore, identification of subjects with critical ventricular geometry, i.e. small horn radii, or increased cardiovascular risk would allow for early intervention via anti-hypertensive therapy [80]. Previous computational models of hydrocephalus have observed elevated interstitial pressure and tissue stress concentrations in the posterior and anterior horns as well [44, 45, 48]. While these models appear similar in the simulation approach, our primary interest in quantifying the cellular stretches of ependymal cells forming the ventricular wall is distinctly different.

Our modeling approach is not without limitations. We select a representative axial slice showing the largest cross-sectional area of the lateral ventricles in order to create subject-specific two-dimensional finite element models. As shown in Figure 3, lateral ventricles have a complex geometry and are subject to three-dimensional loading [49]. Even though we expect differences in the simulated deformation field between a 2D and 3D model, peak ependymal stretches will always appear in locations with high curvature, see Figure 7. Therefore, we anticipate that a 3D model would provide high cell stretches for cells lining the lateral sides of the lateral ventricles which would provide a more accurate overlap with WMHs observed in subjects with enlarged ventricles, see 3D reconstructions of WMHs in Figure 3. Next steps should aim at generating volumetric models to assess the full deformation field of the lateral ventricles. Secondly, we currently do not consider changes in mechanical properties associated with brain aging [81]. Neurodegeneration is associated with tissue softening of gray and white matter [82]. As indicated by our parameter sensitivity analysis, tissue softening leads to increased cell stretch, which is likely a major contributor to pvWMH volume growth. Future models should account for these changes in order to increase the predictive capabilities of our approach. Lastly, we assess ependymal cell stretch via a quasi-static loading case instead of studying the dynamic effects of CSF flow in the ventricles and pulsatile motion from the hemodynamic cycle. The lack of *in vivo* data on the ventricular wall motion, however, is a major limitation to validating a dynamic simulation [47]. To further establish the role of mechanics in the onset and progression of pvWMHs, future work should look into the quantification of *in vivo* wall motion via novel MRI techniques [55] and a histological analysis of the ventricular wall’s temporal decay.

In conclusion, our model is a first step in formulating a unifying theory for a physics-driven mechanism that explains the onset location of pvWMHs in the aging brain. We observe a mechanical loading state of the ventricular wall that causes ependymal cells to be *stretched thin* during each hemodynamic cycle. This particular loading state represents a major risk factor for cellular damage and functional and structural failure of the ventricular wall as it is repeatedly observed in pathology and histological studies on wall damage in aged brains. While vascular damage is a key contributor to pvWMHs, the consistent initial appearance as caps in the ventricular horns, is strongly indicative of a mechanical contribution to ventricular wall failure. We therefore suggest further investigation into the concise etiology and progression of pvWMHs and its prevention strategies.

Acknowledgments

This work was supported by the National Institute of Biomedical Imaging and Bioengineering of the National Institutes of Health under award U24EB028980 to Henry Rusinek for developing the FireVoxel software and the National Institute on Aging of the National Institutes of Health under award R21AG067442 to Johannes Weickenmeier. MRI and clinical data were obtained from the Alzheimer’s Disease Research Center supported by the National Institute on Aging of the National Institutes of Health under award P30AG066512.

Author Contributions

H.R. and J.W. designed the research; V.L.V., H.R., and J.W. performed the research; and V.L.V., H.R., and J.W. wrote the paper.

Competing Interests

All authors have no competing interests.

References

- [1] Franz Fazekas, John B Chawluk, Abass Alavi, Howard I Hurtig, and Robert A Zimmerman. Mr signal abnormalities at 1.5 t in alzheimer’s dementia and normal aging. *American journal of roentgenology*, 149(2):351–356, 1987.

- [2] Joanna M Wardlaw, Eric E Smith, Geert J Biessels, Charlotte Cordonnier, Franz Fazekas, Richard Frayne, Richard I Lindley, John T O'Brien, Frederik Barkhof, Oscar R Benavente, et al. Neuroimaging standards for research into small vessel disease and its contribution to ageing and neurodegeneration. *The Lancet Neurology*, 12(8):822–838, 2013.
- [3] Joanna M Wardlaw, Maria C Valdés Hernández, and Susana Muñoz-Maniega. What are white matter hyperintensities made of? relevance to vascular cognitive impairment. *Journal of the American Heart Association*, 4(6):e001140, 2015.
- [4] FE De Leeuw, Jan Cees de Groot, E Achten, Matthijs Oudkerk, LMP Ramos, R Heijboer, A Hofman, J Jolles, J Van Gijn, and MMB Breteler. Prevalence of cerebral white matter lesions in elderly people: a population based magnetic resonance imaging study. the rotterdam scan study. *Journal of Neurology, Neurosurgery & Psychiatry*, 70(1):9–14, 2001.
- [5] Jessica Alber, Suvarna Alladi, Hee-Joon Bae, David A Barton, Laurel A Beckett, Joanne M Bell, Sara E Berman, Geert Jan Biessels, Sandra E Black, Isabelle Bos, et al. White matter hyperintensities in vascular contributions to cognitive impairment and dementia (vcid): knowledge gaps and opportunities. *Alzheimer's & Dementia: Translational Research & Clinical Interventions*, 5:107–117, 2019.
- [6] J.M. Wardlaw, P.A.G. Sandercock, M.S. Dennis, and J. Starr. Is breakdown of the blood-brain barrier responsible for lacunar stroke, leukoaraiosis, and dementia? *Stroke*, 34(3):806–812, 2003.
- [7] Paul Schmidt, Christian Gaser, Milan Arsic, Dorothea Buck, Annette Förchler, Achim Berthele, Muna Hoshi, Rüdiger Ilg, Volker J Schmid, Claus Zimmer, et al. An automated tool for detection of flair-hyperintense white-matter lesions in multiple sclerosis. *Neuroimage*, 59(4):3774–3783, 2012.
- [8] Kerstin Bendfeldt, Jan Ole Blumhagen, Hanspeter Egger, Patrick Loetscher, Niklaus Denier, Pascal Kuster, Stefan Traud, Nicole Mueller-Lenke, Yvonne Naegelin, Achim Gass, et al. Spatiotemporal distribution pattern of white matter lesion volumes and their association with regional grey matter volume reductions in relapsing-remitting multiple sclerosis. *Human brain mapping*, 31(10):1542–1555, 2010.
- [9] Chun Yu Cheng, Hao Min Cheng, Shih Pin Chen, Chih Ping Chung, Yung Yang Lin, Han Hwa Hu, Chen Huan Chen, and Shuu Jiun Wang. White matter hyperintensities in migraine: Clinical significance and central pulsatile hemodynamic correlates. *Cephalalgia*, 38(7):1225–1236, jun 2018.
- [10] Alida A Gouw, Wiesje M Van Der Flier, Franz Fazekas, Elisabeth C W Van Straaten, Leonardo Pantoni, Anna Poggesi, Domenico Inzitari, Timo Erkinjuntti, Lars O Wahlund, Gunhild Waldemar, Reinhold Schmidt, Philip Scheltens, and Frederik Barkhof. Progression of White Matter Hyperintensities and Incidence of New Lacunes Over a 3-Year Period The Leukoaraiosis and Disability Study. *Stroke*, 39:1414–1420, 2008.
- [11] Hitoshi Fukuda and Mitsuhiro Kitani. Cigarette Smoking Is Correlated With the Periventricular Hyperintensity Grade on Brain Magnetic Resonance Imaging. *Stroke*, 27(4):645–649, apr 1996.
- [12] Sung Hun Kim, Chang Ho Yun, Seo Young Lee, Kyung Ho Choi, Min Bom Kim, and Hee Kwon Park. Age-dependent association between cigarette smoking on white matter hyperintensities. *Neurological Sciences*, 33(1):45–51, feb 2012.
- [13] Hafsa Suhail Najim Al-Anbari, Dawser K Ismail, Mohammed Khudair Hasan, Qutaiba Ahmed Al Khames Aga, Pottathil Shinu, and Anroop B Nair. High blood lead levels: An increased risk for development of brain hyperintensities among type 2 diabetes mellitus patients. *Biological Trace Element Research*, 4:1–9, 2020.
- [14] Karen A. Nunley, Christopher M. Ryan, Trevor J. Orchard, Howard J. Aizenstein, J. Richard Jennings, John Ryan, Janice C. Zgibor, Robert M. Boudreau, Tina Costacou, John D. Maynard, Rachel G. Miller, and Caterina Rosano. White matter hyperintensities in middle-aged adults with childhood-onset type 1 diabetes. *Neurology*, 84(20):2062–2069, 2015.

- [15] Woo-Jin Lee, Keun-Hwa Jung, Young Jin Ryu, Jeong-Min Kim, Soon-Tae Lee, Kon Chu, Manho Kim, Sang Kun Lee, and Jae-Kyu Roh. Association of Cardiac Hemodynamic Factors With Severity of White Matter Hyperintensities in Chronic Valvular Heart Disease. *JAMA Neurology*, 75(1):80–87, 01 2018.
- [16] Charles DeCarli, Evan Fletcher, Vincent Ramey, Danielle Harvey, and William J. Jagust. Anatomical mapping of white matter hyperintensities (wmh). *Stroke*, 36(1):50–55, 2005.
- [17] Christian Lambert, Philip Benjamin, Eva Zeestraten, Andrew J Lawrence, Thomas R Barrick, and Hugh S Markus. Longitudinal patterns of leukoaraiosis and brain atrophy in symptomatic small vessel disease. *Brain*, 139(4):1136–1151, 2016.
- [18] Malee S Fernando, Julie E Simpson, Fiona Matthews, Carol Brayne, Claire E Lewis, Robert Barber, Raj N Kalaria, Gill Forster, Filomena Esteves, Stephen B Wharton, et al. White matter lesions in an unselected cohort of the elderly: molecular pathology suggests origin from chronic hypoperfusion injury. *Stroke*, 37(6):1391–1398, 2006.
- [19] Mohamad Habes, Guray Erus, Jon B Toledo, Tianhao Zhang, Nick Bryan, Lenore J Launer, Yves Rosseel, Deborah Janowitz, Jimit Doshi, Sandra Van der Auwera, et al. White matter hyperintensities and imaging patterns of brain ageing in the general population. *Brain*, 139(4):1164–1179, 2016.
- [20] Ari Ylikoski, Timo Erkinjuntti, Raili Raininko, Seppo Sarna, Raimo Sulkava, and Reijo Tilvis. White matter hyperintensities on mri in the neurologically nondiseased elderly: analysis of cohorts of consecutive subjects aged 55 to 85 years living at home. *Stroke*, 26(7):1171–1177, 1995.
- [21] Franz Fazekas, Stefan Ropele, Christian Enzinger, Faton Gorani, Alexandra Seewann, Katja Petrovic, and Reinhold Schmidt. Mti of white matter hyperintensities. *Brain*, 128(12):2926–2932, 2005.
- [22] Wei Wen, Perminder S Sachdev, Jason J Li, Xiaohua Chen, and Kaarin J Anstey. White matter hyperintensities in the forties: their prevalence and topography in an epidemiological sample aged 44–48. *Human brain mapping*, 30(4):1155–1167, 2009.
- [23] Wei Wen and Perminder Sachdev. The topography of white matter hyperintensities on brain mri in healthy 60-to 64-year-old individuals. *Neuroimage*, 22(1):144–154, 2004.
- [24] Hedvig Söderlund, Lars Nyberg, Rolf Adolfsson, Lars-Göran Nilsson, and Lenore J Launer. High prevalence of white matter hyperintensities in normal aging: relation to blood pressure and cognition. *Cortex*, 39(4-5):1093–1105, 2003.
- [25] Ming-Liang Wang, Xiao-Xing Zhang, Meng-Meng Yu, Wen-Bin Li, and Yue-Hua Li. Prevalence of white matter hyperintensity in young clinical patients. *American Journal of Roentgenology*, 213(3):667–671, 2019.
- [26] Jan Cees De Groot, Frank-Erik De Leeuw, Matthijs Oudkerk, Jan Van Gijn, Albert Hofman, Jellemer Jolles, and Monique MB Breteler. Periventricular cerebral white matter lesions predict rate of cognitive decline. *Annals of neurology*, 52(3):335–341, 2002.
- [27] Reinhold Schmidt, Stefan Ropele, Christian Enzinger, Katja Petrovic, Stephen Smith, Helena Schmidt, Paul M Matthews, and Franz Fazekas. White matter lesion progression, brain atrophy, and cognitive decline: the austrian stroke prevention study. *Annals of Neurology: Official Journal of the American Neurological Association and the Child Neurology Society*, 58(4):610–616, 2005.
- [28] Mandip S Dhamoon, Ying-Kuen Cheung, Ahmet Bagci, Noam Alperin, Ralph L Sacco, Mitchell SV Elkind, and Clinton B Wright. Periventricular white matter hyperintensities and functional decline. *Journal of the American Geriatrics Society*, 66(1):113–119, 2018.
- [29] Marco Duering, Endy Csanadi, Benno Gesierich, Eric Jouvent, Dominique Herve, Stephan Seiler, Boubakeur Belaroussi, Stefan Ropele, Reinhold Schmidt, Hugues Chabriat, et al. Incident lacunes preferentially localize to the edge of white matter hyperintensities: insights into the pathophysiology of cerebral small vessel disease. *Brain*, 136(9):2717–2726, 2013.

- [30] Niels D. Prins and Philip Scheltens. White matter hyperintensities, cognitive impairment and dementia: an update. *Nature Reviews Neurology*, 11:157–165, 2015.
- [31] Ki Woong Kim, James R. MacFall, and Martha E. Payne. Classification of white matter lesions on magnetic resonance imaging in elderly persons. *Biological Psychiatry*, 64(4):273 – 280, 2008.
- [32] Antonio J. Jiménez, María Dolores Domínguez-Pinos, María M. Guerra, Pedro Fernández-Llebreg, and José Manue Pérez-Fígares. Structure and function of the ependymal barrier and diseases associated with ependyma disruption, 2014.
- [33] Cristian Oliver, César A González, Genaro Alvial, Carlos A Flores, Esteban M Rodríguez, and Luis Federico Bátiz. Disruption of cdh2/n-cadherin-based adherens junctions leads to apoptosis of ependymal cells and denudation of brain ventricular walls. *Journal of Neuropathology & Experimental Neurology*, 72(9):846–860, 2013.
- [34] Dale Hatrock, Nina Caporicci-Dinucci, and Jo Anne Stratton. Ependymal cells and multiple sclerosis: proposing a relationship. *Neural regeneration research*, 15(2):263, 2020.
- [35] F. Fazekas, R. Kleinert, and H. Offenbacher. Pathologic correlates of incidental mri white matter signal hyperintensities. *Neurology*, 43(9):1683–1683, 1993.
- [36] Sandra Black, FuQiang Gao, and Juan Bilbao. Understanding white matter disease. *Stroke*, 40(3_suppl.1):S48–S52, 2009.
- [37] JE Simpson, MS Fernando, L Clark, PG Ince, F Matthews, G Forster, JT O’Brien, R Barber, RN Kalaria, C Brayne, et al. White matter lesions in an unselected cohort of the elderly: astrocytic, microglial and oligodendrocyte precursor cell responses. *Neuropathology and applied neurobiology*, 33(4):410–419, 2007.
- [38] Ruth Roales-Buján, Patricia Páez, Montserrat Guerra, Sara Rodríguez, Karin Vío, Ailec Ho-Plagaro, María García-Bonilla, Luis-Manuel Rodríguez-Pérez, María-Dolores Domínguez-Pinos, Esteban-Martín Rodríguez, et al. Astrocytes acquire morphological and functional characteristics of ependymal cells following disruption of ependyma in hydrocephalus. *Acta neuropathologica*, 124(4):531–546, 2012.
- [39] Perminder Sachdev, Wei Wen, Xiaohua Chen, and Henry Brodaty. Progression of white matter hyperintensities in elderly individuals over 3 years. *Neurology*, 68(3):214–222, 2007.
- [40] Alfredo Quiñones-Hinojosa, Nader Sanai, Mario Soriano-Navarro, Oscar Gonzalez-Perez, Zaman Mirzadeh, Sara Gil-Perotin, Richard Romero-Rodriguez, Mitchell S Berger, Jose Manuel Garcia-Verdugo, and Arturo Alvarez-Buylla. Cellular composition and cytoarchitecture of the adult human subventricular zone: a niche of neural stem cells. *Journal of Comparative Neurology*, 494(3):415–434, 2006.
- [41] José L Venero, María L Vizuete, Alberto Machado, and Josefina Cano. Aquaporins in the central nervous system. *Progress in neurobiology*, 63(3):321–336, 2001.
- [42] Orin Bloch, Kurtis I Auguste, Geoffrey T Manley, and AS Verkman. Accelerated progression of kaolin-induced hydrocephalus in aquaporin-4-deficient mice. *Journal of Cerebral Blood Flow & Metabolism*, 26(12):1527–1537, 2006.
- [43] Thomas H. Milhorat, Ronald G. Clark, Mary K. Hammock, and Philip P. McGrath. Structural, Ultrastructural, and Permeability Changes in the Ependyma and Surrounding Brain Favoring Equilibration in Progressive Hydrocephalus. *Archives of Neurology*, 22(5):397–407, 1970.
- [44] Tatsuya Nagashima, Norihiko Tamaki, Satoshi Matsumoto, Barry Horwitz, and Yasuyuki Seguchi. Biomechanics of hydrocephalus: a new theoretical model. *Neurosurgery*, 21(6):898–904, 1987.
- [45] Alonso Pena, Malcolm D Bolton, Helen Whitehouse, and John D Pickard. Effects of brain ventricular shape on periventricular biomechanics: a finite-element analysis. *Neurosurgery*, 45(1):107–118, 1999.

- [46] Zeike Taylor and Karol Miller. Reassessment of brain elasticity for analysis of biomechanisms of hydrocephalus. *Journal of biomechanics*, 37(8):1263–1269, 2004.
- [47] Richard D Penn, Sukhraaj Basati, Brian Sweetman, Xiaodong Guo, and Andreas Linninger. Ventricle wall movements and cerebrospinal fluid flow in hydrocephalus. *Journal of neurosurgery*, 115(1):159–164, 2011.
- [48] Shaokoon Cheng and Lynne E Bilston. Computational model of the cerebral ventricles in hydrocephalus. *Journal of biomechanical engineering*, 132(5), 2010.
- [49] Zhou Zhou, Xiaogai Li, and Svein Kleiven. Biomechanics of periventricular injury. *Journal of neurotrauma*, 37(8):1074–1090, 2020.
- [50] Nityanand Miskin, Hersh Patel, Ana M. Franceschi, Benjamin Ades-Aron, Alexander Le, Brianna E. Damadian, Christian Stanton, Yafell Serulle, James Golomb, Oded Gonen, Henry Rusinek, and Ajax E. George. Diagnosis of normal-pressure hydrocephalus: Use of traditional measures in the era of volumetric MR imaging. *Radiology*, 285(1):197–205, oct 2017.
- [51] Jingyun Chen, Artem V. Mikheev, Han Yu, Matthew D. Gruen, Henry Rusinek, and Yulin Ge. Bilateral distance partition of periventricular and deep white matter hyperintensities: Performance of the method in the aging brain. *Academic Radiology*, 29, 2020.
- [52] J Weickenmeier, M Itskov, Edoardo Mazza, and M Jabareen. A physically motivated constitutive model for 3d numerical simulation of skeletal muscles. *International journal for numerical methods in biomedical engineering*, 30(5):545–562, 2014.
- [53] J Weickenmeier, CAM Butler, PG Young, Alain Goriely, and E Kuhl. The mechanics of decompressive craniectomy: Personalized simulations. *Computer Methods in Applied Mechanics and Engineering*, 314:180–195, 2017.
- [54] Johannes Weickenmeier, Ellen Kuhl, and Alain Goriely. Multiphysics of prionlike diseases: Progression and atrophy. *Physical review letters*, 121(15):158101, 2018.
- [55] Javid Abderezaei, John Martinez, Itamar Terem, Gloria Fabris, Aymeric Pionteck, Yang Yang, Samantha J Holdsworth, Kambiz Nael, and Mehmet Kurt. Amplified flow imaging (aflow): A novel mri-based tool to unravel the coupled dynamics between the human brain and cerebrovasculature. *IEEE Transactions on Medical Imaging*, 39, 2020.
- [56] Samantha J. Holdsworth, Mahdi Salmani Rahimi, Wendy W. Ni, Greg Zaharchuk, and Michael E. Moseley. Amplified magnetic resonance imaging (amri). *Magnetic Resonance in Medicine*, 75(6):2245–2254, 2016.
- [57] Andreas A Linninger, Cristian Tsakiris, David C Zhu, Michalis Xenos, Peter Roycewicz, Zachary Danziger, and Richard Penn. Pulsatile cerebrospinal fluid dynamics in the human brain. *IEEE Transactions on Biomedical Engineering*, 52(4):557–565, 2005.
- [58] David C. Zhu, Michalis Xenos, Andreas A. Linninger, and Richard D. Penn. Dynamics of lateral ventricle and cerebrospinal fluid in normal and hydrocephalic brains. *Journal of Magnetic Resonance Imaging*, 24(4):756–770, 2006.
- [59] William E Butler, Pankaj K Agarwalla, and Patrick Codd. CSF in the ventricles of the brain behaves as a relay medium for arteriovenous pulse wave phase coupling. *PLoS ONE*, 12, 2017.
- [60] Xiaodong Zhong, Craig H. Meyer, David J. Schlesinger, Jason P. Sheehan, Frederick H. Epstein, James M. Larner, Stanley H. Benedict, Paul W. Read, Ke Sheng, and Jing Cai. Tracking brain motion during the cardiac cycle using spiral cine-DENSE MRI. *Medical Physics*, 36(8):3413–3419, 2009.
- [61] J. Weickenmeier, R. de Rooij, S. Budday, P. Steinmann, T.C. Ovaert, and E. Kuhl. Brain stiffness increases with myelin content. *Acta Biomaterialia*, 42:265 – 272, 2016.

- [62] Stephen John Connolly, Donald Mackenzie, and Yevgen Gorash. Isotropic hyperelasticity in principal stretches: explicit elasticity tensors and numerical implementation. *Computational Mechanics*, 64(5):1273–1288, 2019.
- [63] J.A.W. van Dommelen, T.P.J. van der Sande, M. Hrapko, and G.W.M. Peters. Mechanical properties of brain tissue by indentation: Interregional variation. *Journal of the Mechanical Behavior of Biomedical Materials*, 3(2):158 – 166, 2010.
- [64] Silvia Budday, Richard Nay, Rijk de Rooij, Paul Steinmann, Thomas Wyrobek, Timothy C. Ovaert, and Ellen Kuhl. Mechanical properties of gray and white matter brain tissue by indentation. *Journal of the Mechanical Behavior of Biomedical Materials*, 46:318 – 330, 2015.
- [65] T. Kaster, I. Sack, and A. Samani. Measurement of the hyperelastic properties of ex vivo brain tissue slices. *Journal of Biomechanics*, 44(6):1158 – 1163, 2011.
- [66] Naftali Raz, Yiqin Yang, Cheryl L. Dahle, and Susan Land. Volume of white matter hyperintensities in healthy adults: Contribution of age, vascular risk factors, and inflammation-related genetic variants. *Biochimica et Biophysica Acta - Molecular Basis of Disease*, 1822(3):361–369, 2012.
- [67] Leonardo Rangel-Castillo, Shankar Gopinath, and Claudia S Robertson. Management of intracranial hypertension. *Neurologic clinics*, 26(2):521–541, 2008.
- [68] KENNETH SHULMAN and ANTHONY MARMAROU. Analysis of intracranial pressure in hydrocephalus. *Developmental Medicine & Child Neurology*, 10:11–16, 1968.
- [69] Andreas A Linninger, Michalis Xenos, Brian Sweetman, Sukruti Ponkshe, Xiaodong Guo, and Richard Penn. A mathematical model of blood, cerebrospinal fluid and brain dynamics. *Journal of mathematical biology*, 59(6):729–759, 2009.
- [70] S Budday, Gerhard Sommer, C Birkl, C Langkammer, J Haybaeck, J Kohnert, M Bauer, F Paulsen, P Steinmann, E Kuhl, et al. Mechanical characterization of human brain tissue. *Acta biomaterialia*, 48:319–340, 2017.
- [71] Reginald Hooper. Hydrocephalus and obstruction of the superior vena cava in infancy. *Pediatrics*, 28(5), 1961.
- [72] Kenneth Shulman and Anthony Marmarou. Analysis of Intracranial Pressure in Hydrocephalus. *Developmental Medicine & Child Neurology*, 10:11–16, nov 2008.
- [73] Pauline Maillard, Sudha Seshadri, Alexa Beiser, Jayandra J Himali, Rhoda Au, Evan Fletcher, Owen Carmichael, Philip A Wolf, and Charles DeCarli. Effects of systolic blood pressure on white-matter integrity in young adults in the framingham heart study: a cross-sectional study. *The Lancet Neurology*, 11(12):1039–1047, 2012.
- [74] Brett A Shook, Jessica B Lenington, Rebecca L Acabchuk, Meredith Halling, Ye Sun, John Peters, Qian Wu, Amit Mahajan, Douglas W Fellows, and Joanne C Conover. Ventriculomegaly associated with ependymal gliosis and declines in barrier integrity in the aging human and mouse brain. *Aging cell*, 13(2):340–350, 2014.
- [75] Krysti L Todd, Tessa Brighton, Emily S Norton, Samuel Schick, Wendy Elkins, Olga Pletnikova, Richard H Fortinsky, Juan C Troncoso, Peter J Molfese, Susan M Resnick, et al. Ventricular and periventricular anomalies in the aging and cognitively impaired brain. *Frontiers in Aging Neuroscience*, 9:445, 2018.
- [76] L Noël and E Kuhl. Modeling neurodegeneration in chronic traumatic encephalopathy using gradient damage models. *Computational Mechanics*, 64(5):1375–1387, 2019.
- [77] Johnny Wang, Maria J Knol, Aleksei Tiulpin, Florian Dubost, Marleen de Bruijne, Meike W Vernooij, Hieab HH Adams, M Arfan Ikram, Wiros J Niessen, and Gennady V Roshchupkin. Gray matter age prediction as a biomarker for risk of dementia. *Proceedings of the National Academy of Sciences*, 116(42):21213–21218, 2019.

- [78] Dominic Holland, James B Brewer, Donald J Hagler, Christine Fennema-Notestine, Anders M Dale, Alzheimer's Disease Neuroimaging Initiative, et al. Subregional neuroanatomical change as a biomarker for alzheimer's disease. *Proceedings of the National Academy of Sciences*, 106(49):20954–20959, 2009.
- [79] Joshua Chiappelli, Laura M Rowland, S Andrea Wijtenburg, Hongji Chen, Andrew A Maudsley, Sulaiman Sheriff, Shuo Chen, Anya Savransky, Wyatt Marshall, Meghann C Ryan, et al. Cardiovascular risks impact human brain n-acetylaspartate in regionally specific patterns. *Proceedings of the National Academy of Sciences*, 116(50):25243–25249, 2019.
- [80] Aditi Gupta, Sophy Perdomo, Sandra Billinger, Srinivasan Beddhu, Jeffrey Burns, and Gary Gronseth. Treatment of hypertension reduces cognitive decline in older adults: a systematic review and meta-analysis. *BMJ open*, 10(11):e038971, 2020.
- [81] Ingolf Sack, Bernd Beierbach, Jens Wuerfel, Dieter Klatt, Uwe Hamhaber, Sebastian Papazoglou, Peter Martus, and JÃ¼rgen Braun. The impact of aging and gender on brain viscoelasticity. *NeuroImage*, 46(3):652 – 657, 2009.
- [82] Matthew C Murphy, John Huston III, Clifford R Jack Jr, Kevin J Glaser, Armando Manduca, Joel P Felmlee, and Richard L Ehman. Decreased brain stiffness in alzheimer's disease determined by magnetic resonance elastography. *Journal of magnetic resonance imaging*, 34(3):494–498, 2011.